

Memristive effect on a Hindmarsh-Rose neuron

Fei Gao(高飞), Xiangcheng Yu(于相成), Yue Deng(邓玥), Fang Yuan(袁方), Guangyi Wang(王光义), and Tengfei Lei(雷腾飞)

Citation: Chin. Phys. B, 2025, 34 (**12**): 120504. DOI: 10.1088/1674-1056/ae0b3a
http://cpb.iphy.ac.cn; http://iopscience.iop.org/cpb

What follows is a list of articles you may be interested in

Chaos of cavity optomechanical system with Coulomb coupling

Yingjia Yang(杨应佳), Liwei Liu(刘利伟), Lianchun Yu(俞连春), Weizheng Kong(孔伟正), Haiyan Jiao(焦海燕), Xiaoyan Deng(邓小燕), and Xiaoyong Li(李小勇)

Chin. Phys. B, 2025, 34 (**8**): 080503. DOI: 10.1088/1674-1056/add509

Generation of multitype, multicavity chaotic attractors via impulse-function-based state variable extension

Xiaoyu Hu(胡晓宇), Siteng Wang(王思腾), Panpan Wu(邬盼盼), Hongbo Cao(曹红博), Tianwei Yang(杨天纬), and Zhongshuo Dong(董忠硕)

Chin. Phys. B, 2025, 34 (**8**): 080502. DOI: 10.1088/1674-1056/add249

Complexity dynamics analysis of a dual-channel green supply chain with government intervention and cap-and-trade regulation

Yuhao Zhang(张玉豪), Lin Huang(黄林), and Man Yang(杨满)

Chin. Phys. B, 2025, 34 (**7**): 070501. DOI: 10.1088/1674-1056/adca9c

Resonant tunneling diode cellular neural network with memristor coupling and its application in police forensic digital image protection

Fei Yu(余飞), Dan Su(苏丹), Shaoqi He(何邵祁), Yiya Wu(吴亦雅), Shankou Zhang(张善扣), and Huige Yin(尹挥戈)

Chin. Phys. B, 2025, 34 (**5**): 050502. DOI: 10.1088/1674-1056/adb8bb

Model-free prediction of chaotic dynamics with parameter-aware reservoir computing

Jianmin Guo(郭建敏), Yao Du(杜瑶), Haibo Luo(罗海波), Xuan Wang(王晅), Yizhen Yu(于一真), and Xingang Wang(王新刚)

Chin. Phys. B, 2025, 34 (**4**): 040505. DOI: 10.1088/1674-1056/adb733

SPECIAL TOPIC — Biophysical circuits: Modeling & applications in neuroscience

Memristive effect on a Hindmarsh–Rose neuron

Fei Gao(高飞)[1], Xiangcheng Yu(于相成)[2], Yue Deng(邓玥)[2], Fang Yuan(袁方)[2], Guangyi Wang(王光义)[1], and Tengfei Lei(雷腾飞)[1,†]

[1] *Jinan Key Laboratory of Memristive Computing and Applications (JKLMCA), Qilu Institute of Technology, Jinan* 250200, *China*
[2] *College of Electrical Engineering and Automation, Shandong University of Science and Technology, Qingdao* 266590, *China*

(Received 3 August 2025; revised manuscript received 4 September 2025; accepted manuscript online 25 September 2025)

Considering the impact of electromagnetic induction on neurons, this paper presents a three-dimensional (3D) memristor Hindmarsh–Rose (HR) neuron model. This model exhibits diverse hidden chaotic dynamics due to the absence of equilibrium points, including bifurcation phenomena, coexisting attractors, transient chaos, state transitions, and offset-boosting control. Since equilibrium points are absent in this model, all observed dynamics are classified as hidden behaviors. The complex dynamics of this neuron model are illustrated through bifurcation diagrams, Lyapunov diagrams, time series plots, and phase portraits. Furthermore, an equivalent circuit for the memristor HR neuron is constructed, and the accuracy of numerical simulations is confirmed via circuit simulation results.

Keywords: chaos, memristor, HR neuron, electromagnetic induction, hidden attractor

PACS: 05.45.–a, 87.19.ll, 84.35.+i

DOI: 10.1088/1674-1056/ae0b3a **CSTR:** 32038.14.CPB.ae0b3a

1. Introduction

The brain is a nonlinear behavioral organ that can exhibit extreme complexity.[1] The neuron is the fundamental unit of the central nervous system and can be regarded as both a structural and functional element of the system. Moreover, neurons play a crucial role in information generation, transmission, reception, and processing within the brain. Their electrical activities exhibit intricate nonlinear dynamic behaviors.[2] Various neuron models have been proposed to simulate neuronal electrical activity, including two-dimensional (2D) and three-dimensional (3D) Hindmarsh–Rose (HR) models.[3–7] Furthermore, these HR neuron models provide an effective framework for analyzing neuronal electrical activity due to their relatively simple algebraic structure.

In recent years, it has been recognized that neuronal electrical activity can be influenced by various factors, including network topology,[8] noise,[9] time delay,[10] and electromagnetic radiation. Among these, the impact of electromagnetic radiation cannot be disregarded. With industrial development and technological advancements, individuals are increasingly exposed to machinery, portable electromagnetic devices, and other instruments generating electromagnetic fields. Research indicates that such exposure can enhance mutual electromagnetic interactions within brain cells, potentially leading to neurological disorders such as multiple sclerosis, Alzheimer's disease, migraine, epilepsy, and Parkinson's disease.[11] Additionally, studies have demonstrated that memristors can effectively model the effect of electromotive induction on neuronal membrane potential at the cellular level.[12] Numerous neurons and neural networks constructed with memristors have been reported in the literature, revealing their complex dynamic behaviors.[13–16]

In the field of neural network research, Lin *et al.*[17] investigated the impact of electromagnetic radiation on Hopfield neural networks, showing that these networks can exhibit an infinite number of hidden transient chaotic phenomena. Furthermore, Ref. [18] examined the effect of electromagnetic radiation on coupled small neural networks and revealed hidden coexisting electrical activities through PSPICE simulation. A novel cell neural network (MCNN-CS) incorporating memristors was constructed in Ref. [19], demonstrating that chaotic cell neural networks exhibit rich dynamic characteristics, high sensitivity to initial conditions, and persistent chaotic features. Moreover, a new memristor-based chaotic system (SC-CNN) was proposed in Ref. [20], indicating that CNN cell neural networks can exhibit infinitely coexisting attractors determined by initial values under electromagnetic radiation.

Beyond neural networks, isolated neurons have received considerable attention due to their simple structure and effectiveness in analyzing neuronal activity. For example, Ma *et al.*[21] used memristors to simulate the impact of electromagnetic radiation and found that it can not only stimulate the discharge of resting neurons but also induce more complex dynamic behaviors. Bao *et al.*[22] investigated electromagnetic radiation effects on a 3D HR neuron model with memristors and conducted a detailed analysis of coexisting attractor

†Corresponding author. E-mail: leitengfeicanhe@126.com

© 2025 Chinese Physical Society and IOP Publishing Ltd. All rights, including for text and data mining, AI training, and similar technologies, are reserved.

groups, burst discharges, and their underlying mechanisms.

Similarly, Ref. [23] explored the effects of electromagnetic radiation, revealing heterogeneous extreme multistability and multi-scroll phenomena. These findings underscore the significant influence of electromagnetic radiation on neurons, giving rise to diverse dynamic phenomena. With rapid advancements in nonlinear dynamics and biophysics at the single-neuron level, researchers have initiated studies on multimodal and mode-transition phenomena associated with neuronal electrical activity. For instance, Parastesh *et al.*[24] proposed a discrete fractional-order memristive HR model, showing that chaotic firing depends on both fractional order and magnetic strength, and further investigated synchronization under electrical coupling. Moreover, using memristors as self-connected synapses revealed four coexisting electrical activities along with transient chaos.[25] Hence, there is a pressing need to study multimodal and mode-transition phenomena in neuronal electrical activity.

This paper proposes a memristive HR neuron model incorporating the effects of electromagnetic radiation. The contributions of this study include: (i) development of a physical memristor simulator and validation of its accuracy, providing a theoretical basis for investigating the characteristics of physical memristors. (ii) The proposed memristor HR neuron model lacks equilibrium points, enabling exploration of hidden dynamic phenomena. (iii) Identification of hidden asymmetric attractors and local steady-state chaos phenomena in the memristive HR neuron model. Notably, hidden transient chaotic transitions are also examined, which have not been previously reported in memristive HR neuron models.

The remainder of the paper is organized as follows. Section 2 presents the development of a physical memristor simulator based on the Ti/TiO_{2-x}:Cu/Cu (TTC) nano-memristor mathematical model, with its accuracy verified through Multisim simulations. A novel memristive HR neuron model is also constructed. Section 3 combines theoretical analysis and numerical simulations to examine the dynamic behaviors of the memristive HR neuron model. In Section 4, the proposed neuron model is implemented in Multisim to demonstrate its dynamic behaviors. Finally, conclusions are drawn in Section 5.

2. The model of memristive neuron

2.1. Description of the TTC memristor

In our previous investigations, the TTC nano-memristor was fabricated via magnetron sputtering, and a corresponding mathematical model was established, defined as follows:[26]

$$\begin{cases} i_{\mathrm{m}} = \beta \varphi_{\mathrm{m}} \sinh(\alpha v_{\mathrm{m}}), \\ \dfrac{\mathrm{d}\varphi_{\mathrm{m}}}{\mathrm{d}t} = \mu v_{\mathrm{m}}, \end{cases} \tag{1}$$

where φ_{m} denotes the magnetic flux, and v_{m} and i_{m} represent the voltage across and current through the memristor, respectively. The symbols α, β, and μ are fitting parameters, and t is the integration time constant. By setting $\alpha = 0.8$, $\beta = 0.000125$, and $\mu = 0.535$, and applying a sinusoidal voltage $v_{\mathrm{m}} = V_{\mathrm{m}} \sin(2\pi f t)$ to the memristor, Fig. 1(a) illustrates the resulting V–I characteristic of the memristor. As shown in Fig. 1(a), increasing the frequency of the input sinusoidal signal leads to a reduction in the side-lobe area of the hysteresis curve. When the frequency f is fixed at 0.5 Hz and V_{m} is varied, the V–I curve of the memristor is presented in Fig. 1(b). It is evident that an increase in amplitude results in an enlargement of the hysteresis side-lobe area. These simulation results indicate that the memristor model effectively captures the essential characteristics of memristive behavior.

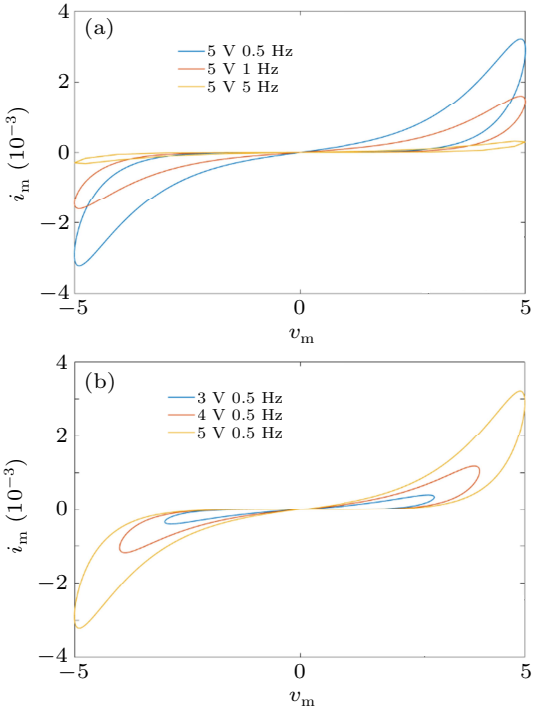


Fig. 1. Pinched hysteresis loops of the TTC memristor under different excitations: (a) varying excitation frequencies f, (b) varying excitation amplitudes V_{m}.

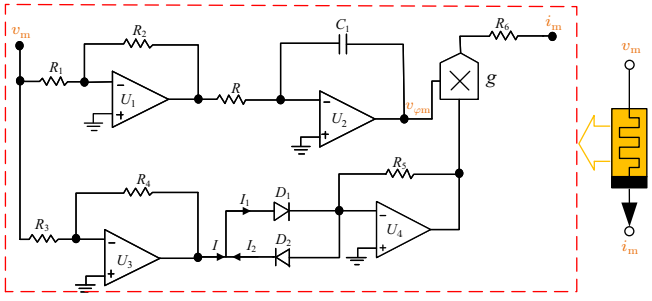


Fig. 2. Schematic diagram of the equivalent circuit for the TTC memristor.

For chaotic systems, the dynamic behavior is highly sensitive to initial conditions, leading to eventual divergence in system states even when the initial values are nearly identical. Previous experiments with physical memristors have faced challenges in precisely setting their initial conditions, limiting the investigation of dynamic phenomena dependent

on these values, such as coexisting attractors and extreme multistability. To address this limitation, we have developed a TTC memristor simulator (Fig. 2) that effectively reproduces the essential characteristics of a TTC memristor using only a minimal set of simulator components.

The circuit comprises resistors, capacitors, diodes (1N4148), a multiplier (AD633JN), and four integrated operational amplifiers (TL082CP). Among these components, U1 is used to control the fitting parameter μ, U2 controls the integration in Eq. (1), U3 controls the fitting parameter α, and U4 controls the fitting parameter β. The multiplier g performs the integration operation on the two-terminal signal. As shown in Fig. 2, the current through each diode can be described using the Shockley diode equation

$$I_{\mathrm{D}} = I_{\mathrm{s}}\left(\mathrm{e}^{\frac{v_{\mathrm{D}}}{nV_{\mathrm{T}}}} - 1\right), \tag{2}$$

where I_{S} is the reverse-bias saturation current, n is the emission coefficient, V_{T} is the thermal voltage, and v_{D} is the voltage across the diode. According to Kirchhoff's current law, the following expression can be obtained

$$\begin{aligned} I = I_1 - I_2 &= I_{\mathrm{s}}\left(\mathrm{e}^{\frac{v_{\mathrm{AB}}}{nV_{\mathrm{T}}}} - 1\right) - I_{\mathrm{s}}\left(\mathrm{e}^{\frac{-v_{\mathrm{AB}}}{nV_{\mathrm{T}}}} - 1\right) \\ &= I_{\mathrm{s}}\left(\mathrm{e}^{\frac{v_{\mathrm{AB}}}{nV_{\mathrm{T}}}} - \mathrm{e}^{\frac{-v_{\mathrm{AB}}}{nV_{\mathrm{T}}}}\right) \\ &= 2I_{\mathrm{s}}\sinh\left(\frac{v_{\mathrm{AB}}}{nV_{\mathrm{T}}}\right). \end{aligned} \tag{3}$$

Based on circuit theory, the governing equation of the memristor simulator can be written as in Eq. (4), where v_{m} and i_{m} denote the voltage and current, and φ_{m} represents the state variable of the memristor simulator

$$\begin{cases} i_{\mathrm{m}} = \dfrac{R_5 g \varphi_{\mathrm{m}}}{R_6} I = 2I_{\mathrm{s}} \dfrac{R_5 g \varphi_{\mathrm{m}}}{R_6} \sinh\left(\dfrac{R_4}{nV_{\mathrm{T}}R_3} v_{\mathrm{m}}\right), \\ C_1 \dfrac{\mathrm{d}\varphi_{\mathrm{m}}}{\mathrm{d}\tau} = \dfrac{R_2}{R_1 R} v_{\mathrm{m}}. \end{cases} \tag{4}$$

Table 1. The experimental variable value of the equivalent circuit of the memristor.

Parameters	Values	Parameters	Values
I_{s}	1 nA	R_3	10 kΩ
V_{T}	26 mV	R_4	0.416 kΩ
n	2	R_5	62.5 MΩ
R	10 kΩ	R_6	10 kΩ
g_1	1	R_2	5.35 kΩ
R_1	10 kΩ		

Equation (4) can be simplified to Eq. (1) by introducing a time scale factor $\tau = RC_1 t$ and defining $\alpha = R_4/(nV_{\mathrm{T}}R_3)$, $\beta = 2I_{\mathrm{S}}R_5 g$, and $\mu = R_2/(R_1 R_0)$. In circuit experiments, the sinusoidal signal $v_{\mathrm{m}} = V_{\mathrm{m}}\sin(2\pi F t)$ is generated using a function generator, with oscillation frequency $F = f/(RC_1)$. When the circuit parameters are set as listed in Table 1, varying input voltages and frequencies produce pinch hysteresis loops corresponding to the numerical simulation results in Fig. 3. The close agreement between numerical simulations and experimental measurements demonstrates the effectiveness of the memristor simulator.

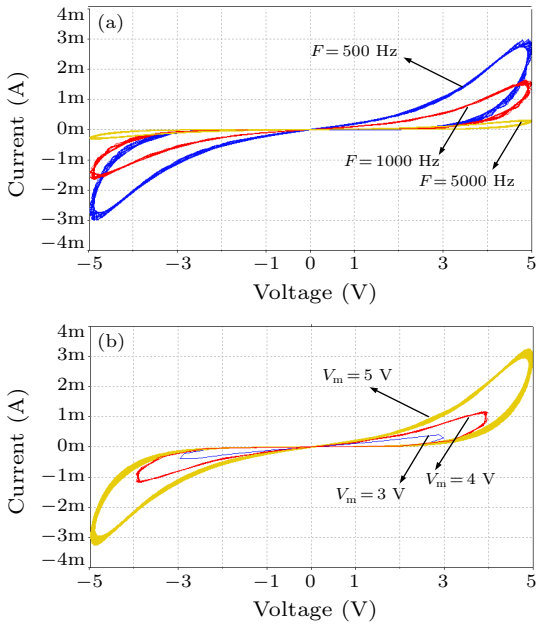


Fig. 3. Pinched hysteresis loops of the TTC memristor under different excitations: (a) varying excitation frequencies F, (b) varying excitation amplitudes V_{m}.

2.2. Memristive HR neuron model

The Hodgkin–Huxley neuron model is a well-established framework that exhibits rich electrical activity. However, its algebraic structure is highly complex. As a result, several simplified neuron models have been developed based on this framework, including the 2D HR neuron model. The 2D HR model provides a straightforward yet effective approach for investigating neuronal dynamics, capable of generating both spikes and bursts of electrical activity. Its mathematical formulation is given by

$$\begin{cases} \dfrac{\mathrm{d}x}{\mathrm{d}t} = y - ax^3 + bx^2 + I, \\ \dfrac{\mathrm{d}y}{\mathrm{d}t} = c - dx^2 - y, \end{cases} \tag{5}$$

where x and y denote the neuron's membrane potential and recovery variables, respectively. The symbol I represents the external stimulus current, and a, b, c, and d are model parameters.

Despite its simplicity, this model is limited to generating basic periodic oscillations, as illustrated in Fig. 4, and cannot capture the complex nonlinear phenomena observed in biological neurons.[27] Furthermore, empirical studies have shown that appropriate electromagnetic radiation can induce chaotic discharge in resting-state neurons, significantly modifying their dynamic behavior. Therefore, it is essential to con-

sider the effects of electromagnetic radiation when extending 2D HR neuron models for more realistic simulations.

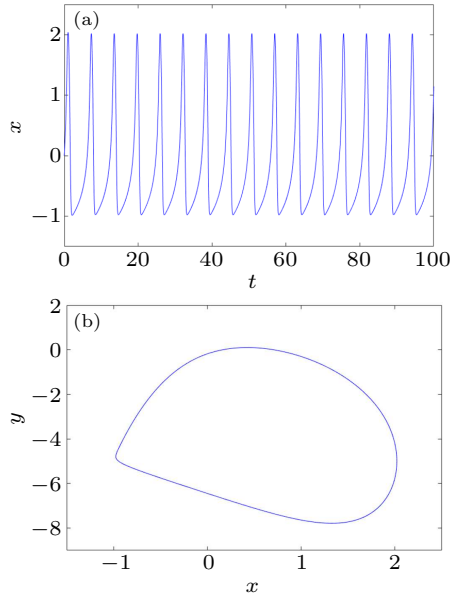


Fig. 4. Firing behavior and phase portrait of the original 2D HR neuron model: (a) time series, (b) phase portrait.

The impact of electromagnetic radiation on an isolated neuron can be characterized by fluctuations in magnetic flux across the cell membrane, as described by Maxwell's equations, while the coupling between magnetic flux and membrane potential can be realized using a magnetically controlled memristor.[28] Based on this concept, we have developed a 3D memristive HR neuron model incorporating electromagnetic induction. The state equations for this memristive HR neuron (MHRN) model are given in Eq. (6). The parameters in the memristive term, α and β, are derived from the physical TTC memristor model, representing the nonlinear ion channel dynamics and the intensity of electromagnetic induction, respectively.[26] The parameter μ denotes the feedback gain from membrane potential to magnetic flux, analogous to the sensitivity of ion channels to changes in the electrical field in biological neurons.[28] This formulation provides a biophysically plausible representation of how electromagnetic fields can modulate neuronal excitability and firing patterns, as observed in studies of neurological disorders[11]

$$\begin{cases} \dfrac{\mathrm{d}x}{\mathrm{d}t} = y - ax^3 + bx^2 + I + \beta\varphi_{\mathrm{m}}\sinh(\alpha x), \\ \dfrac{\mathrm{d}y}{\mathrm{d}t} = c - dx^2 - y, \\ \dfrac{\mathrm{d}\varphi_{\mathrm{m}}}{\mathrm{d}t} = \mu x. \end{cases} \tag{6}$$

Here, φ_{m} represents the magnetic flux through the membrane, $\beta\varphi_{\mathrm{m}}\sinh(\alpha x)$ represents the magnetically induced current, β denotes the electromagnetic induction intensity, and μ represents the feedback effect of membrane potential on the magnetic flux. The adjustable parameters in this MHRN model (6) are I and β, which are restricted to the first quadrant of the parameter space ($I > 0$ and $\beta > 0$). Setting the left-hand side of Eq. (6) to zero shows that an equilibrium point exists only when $I = -c < 0$, which contradicts the condition $I > 0$. Therefore, the system has no equilibrium points, and all generated attractors are hidden.

Compared to other memristive neuron models, such as the FitzHugh–Nagumo or Wilson models,[12–14] which often employ idealized memristive functions, our model is distinguished by its foundation in a physical TTC memristor with a sinh-type nonlinearity. This approach offers two main advantages: first, it provides a more accurate and hardware-realizable representation of electromagnetic induction effects; second, it leads to the emergence of richer and more complex hidden dynamics, including transient chaotic transitions and local constant chaos, which are less commonly reported in models with simpler memristive approximations. These features make our model particularly suitable for investigating the complex nonlinear phenomena induced by electromagnetic radiation in biological neurons.

3. Complex dynamics analysis

3.1. Dynamics varied with I

The parameters of the proposed MHRN model (6) are set as follows: $a = 1$, $b = 3$, $c = 1$, $d = 5$, $\alpha = 0.8$, $\beta = 1.175$, and $\mu = 0.535$. When the parameter I is varied within the range $[0.3, 0.6]$ with the initial condition $(0.6, 0, 0)$, the bifurcation diagram of the membrane potential x is shown in Fig. 5(a). The corresponding first two Lyapunov exponents are depicted in Fig. 5(b), revealing dynamic phenomena such as periodicity, period windowing, period-doubling bifurcation, and the onset of chaos. These results demonstrate that incorporating a memristor into the original two-dimensional HR neuron model (5) leads to more intricate bifurcation behaviors.

As observed in Fig. 5, the bifurcation diagram and Lyapunov spectrum diagram correspond closely, indicating the same ranges of periodic and chaotic dynamics. Starting from $I = 0.3$, the system trajectory briefly passes through a period window near $I = 0.354$ before entering another chaotic region. Subsequently, an inverse period-doubling bifurcation transitions the system from chaos back to periodicity. As I increases further, the system re-enters a chaotic region within $[0.47, 0.5]$, followed by another transition to a periodic state via an inverse period-doubling bifurcation. Additionally, Fig. 6 presents nine distinct attractors corresponding to different values of I, providing clear evidence of this bifurcation process.

3.2. Coexisting attractors

In nonlinear systems, the coexistence of attractors is a common phenomenon, indicating that, by keeping system

parameters fixed while varying the initial conditions, multiple types or shapes of attractors can emerge. In this section, the initial values of the system are set to $(0.6,0,0)$ and $(-5,3,-1)$, respectively. As the parameter I increases from 0.3 to 0.6, the bifurcation diagram of the maximum membrane potential x changes correspondingly, as shown in Fig. 7(a). The maximum Lyapunov exponents are depicted in Fig. 7(b), where the blue trajectory corresponds to the initial condition $(0.6,0,0)$ and the red trajectory corresponds to $(-5,3,-1)$.

From Fig. 7, it is evident that the bifurcation diagram depends sensitively on the initial conditions: the system with initial values $(-5,3,-1)$ exhibits different dynamics compared to $(0.6,0,0)$. This indicates the coexistence of periodic and chaotic attractors, in addition to period-doubling and simple periodic orbits. Numerical simulations in the y–x plane reveal four sets of coexisting attractors at $I = 0.353$, 0.48, 0.505, and 0.55, as illustrated in Fig. 8. Among these trajectories, the blue one corresponds to the initial state $(0.6,0,0)$, while the red trajectory corresponds to $(-5,3,-1)$. Furthermore, Figs. 8(a)–8(c) show three sets of coexisting chaotic and periodic attractors, whereas Fig. 8(d) presents two sets of coexisting periodic attractors. Hence, the memristive HR neuron model (Eq. (6)) can generate multiple types of multi-group coexisting attractors under different initial conditions, demonstrating its high sensitivity to initial values.

3.3. Transient chaotic transition phenomena

Transient chaos refers to trajectories that exhibit chaotic behavior over a finite time interval before settling into a final non-chaotic state, which may be either periodic or stationary.[29] The emergence of transient chaos can be attributed to the gradual convergence between a chaotic attractor and its basin of attraction in phase space as system parameters vary. Upon reaching a critical parameter value, the chaotic attractor may encounter unstable periodic orbits, resulting in a boundary crisis. The occurrence of transient chaos is thus often associated with such boundary crises.

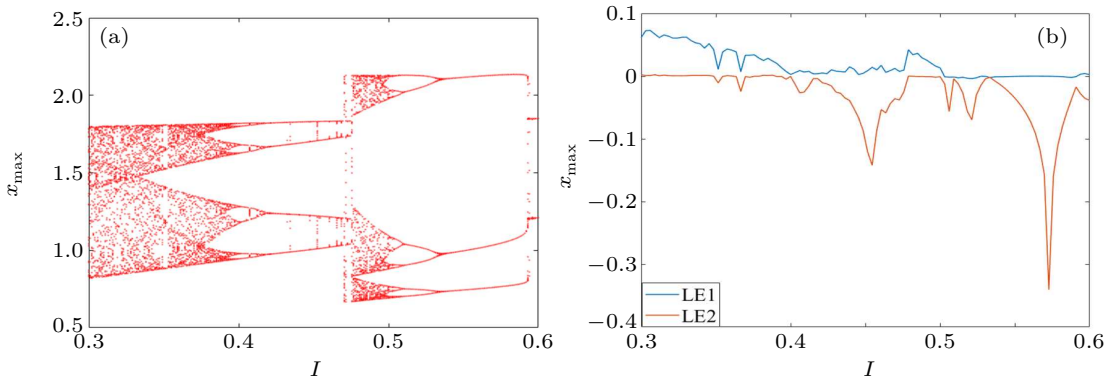


Fig. 5. Bifurcation diagram and Lyapunov exponent spectrum of the system with varying I: (a) bifurcation diagram, (b) Lyapunov exponent spectrum.

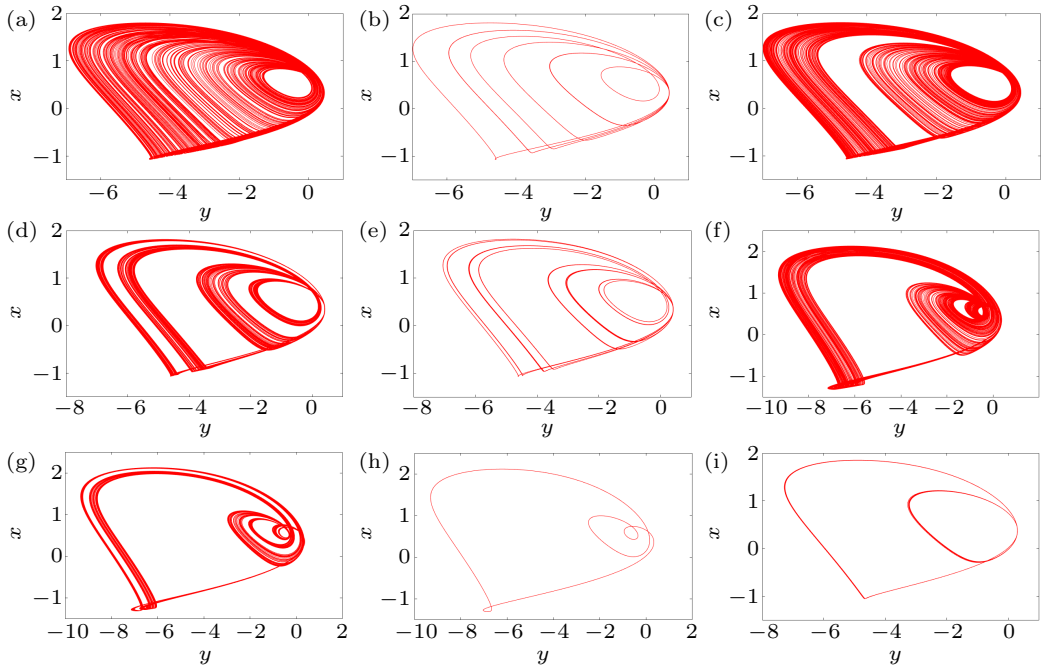


Fig. 6. Phase portraits of the attractors in the y–x plane for different values of I: (a) $I = 0.31$, (b) $I = 0.353$, (c) $I = 0.36$, (d) $I = 0.39$, (e) $I = 0.4$, (f) $I = 0.48$, (g) $I = 0.5$, (h) $I = 0.55$, (i) $I = 0.6$.

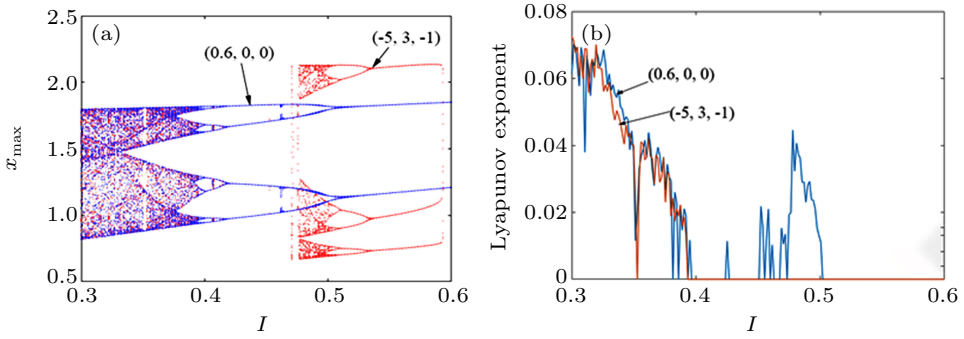


Fig. 7. Coexisting bifurcation behavior of the system with respect to I for different initial conditions: (a) bifurcation diagram, (b) Lyapunov exponent spectrum.

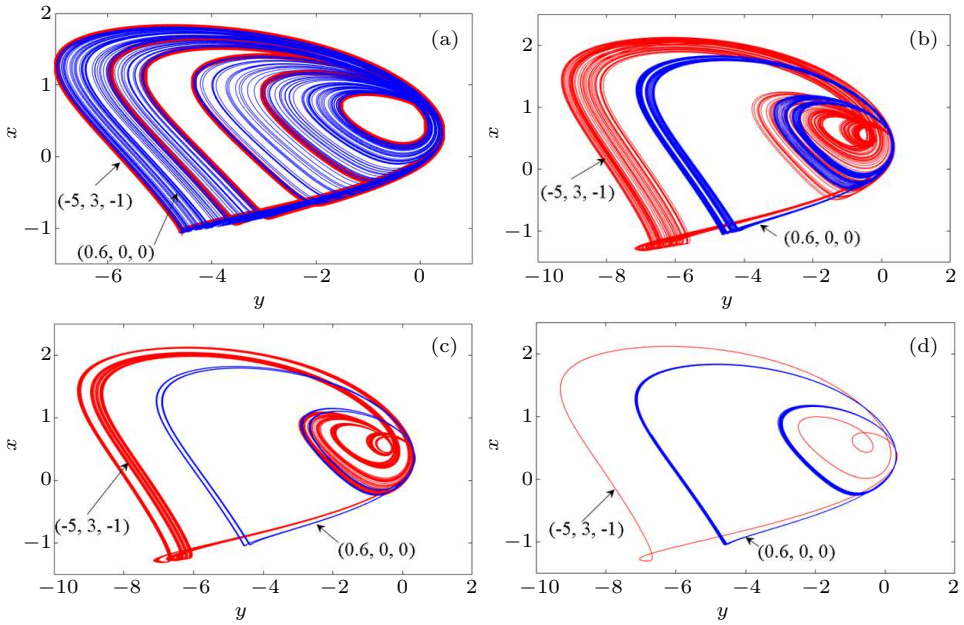


Fig. 8. Phase diagrams of coexisting attractors in the y–x plane for different values of I: (a) $I = 0.353$, (b) $I = 0.48$, (c) $I = 0.5$, (d) $I = 0.55$.

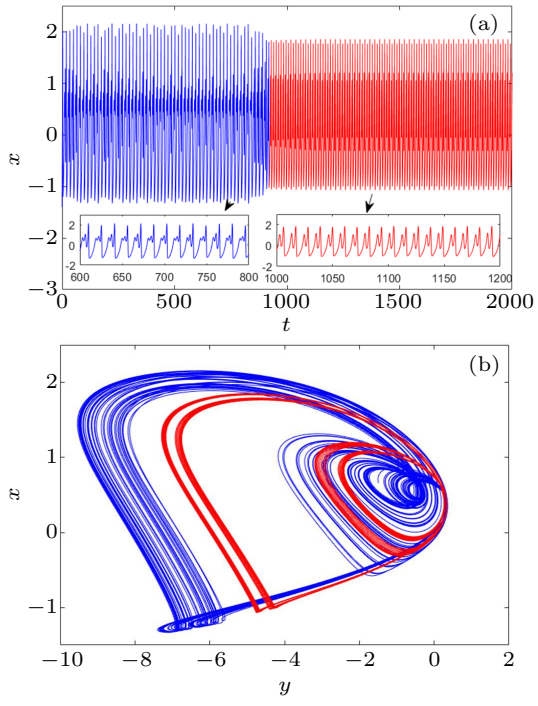


Fig. 9. Transient chaotic phenomenon: (a) time series of membrane potential, (b) corresponding phase diagram.

For example, consider the system parameters $a = 1$, $b = 3$, $c = 1$, $d = 5$, $\alpha = 0.8$, $\beta = 1.195$, $\mu = 0.535$, and $I = 0.512$. Transient chaos occurs when the initial condition is set to $(-1.4, 0, 0)$. In this case, the system trajectory transitions from a chaotic state to a periodic state over time. As shown in Fig. 9(a), the time series of the membrane potential x exhibits chaos within the interval $[0, 900]$, and gradually evolves into periodic behavior for $t > 900$. To further illustrate this transient chaotic behavior, Fig. 9(b) presents the phase portraits in the y–x plane: the blue trajectory corresponds to the chaotic phase within $[0, 900]$, while the red trajectory represents the periodic phase within $[900, 2000]$.

In addition to the previously described transient chaotic phenomena, the system also exhibits transient chaotic transition behavior. When the parameters are set as $a = 1$, $b = 3$, $c = 1$, $d = 5$, $\alpha = 0.8$, $\beta = 1.13$, $\mu = 0.535$, $I = 0.3$, and the initial condition is $(0, 0, 0)$, a transient chaotic transition can be observed. Figure 10(a) illustrates the time series of the membrane potential x, where the transient chaotic interval occurs within $[0, 350]$ and subsequently transitions into another chaotic state for $t > 350$. To further illustrate this

phenomenon, Fig. 10(b) presents the phase portrait in the y–x plane, with the blue trajectory corresponding to the interval $[0,350]$ and the red trajectory representing $[350,800]$. Unlike conventional transient chaos, this unusual transition behavior is highly sensitive to initial conditions, representing a novel dynamic phenomenon.

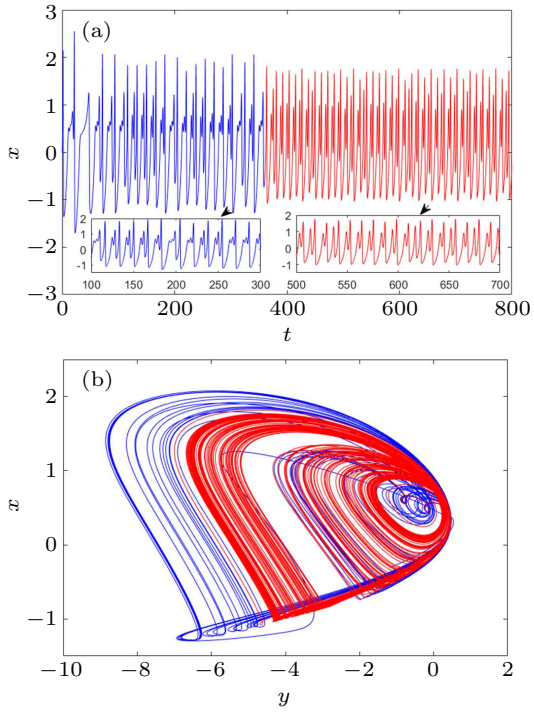


Fig. 10. Transient chaotic transition phenomenon: (a) time series of membrane potential, (b) corresponding phase diagram.

3.4. Local constant chaotic state and state transition caused by initial conditions

When system parameters are fixed, the dynamic behavior can remain chaotic despite variations in initial conditions. This phenomenon is referred to as a locally constant chaotic state. In biological neurons, such sustained chaotic activity may correspond to neural states associated with high-level cognitive processes, such as attention or creative thinking, where a balance between stability and flexibility is essential.

Considering the parameter values $a = 1$, $b = 3$, $c = 1$, $d = 5$, $\alpha = 0.8$, $\beta = 1.25$, $\mu = 0.535$, and $I = 0.1$, and an initial condition of $(x(0),0,0)$, the bifurcation diagram with respect to $x(0)$ is shown in Fig. 11(a). It can be observed that variations in $x(0)$ have minimal impact on the system's dynamics. The corresponding first two Lyapunov exponents are depicted in Fig. 11(b). Within the interval $x(0) \in (-5,5)$, the maximum Lyapunov exponent remains consistently positive, while the sum of all three Lyapunov exponents remains negative and unchanged. These results indicate that the system maintains a locally constant chaotic state within this range.

State switching is defined as a perturbation near a critical point that can induce a qualitative change in the system's dynamic behavior. When system parameters vary, a previously stable chaotic state may be disrupted, leading to state switching. To investigate this phenomenon, the system parameters are set as $a = 1$, $b = 3$, $c = 1$, $d = 5$, $\alpha = 0.8$, $\beta = 1.19$, $\mu = 0.535$, $I = 0.51$, with the initial condition $(x(0),0,0)$. Figure 12 illustrates the bifurcation diagram of the maximum membrane potential x and the corresponding Lyapunov spectrum within the range $x(0) \in [-3.25,3.25]$. The figure demonstrates alternating transitions between periodic and $x(0)$

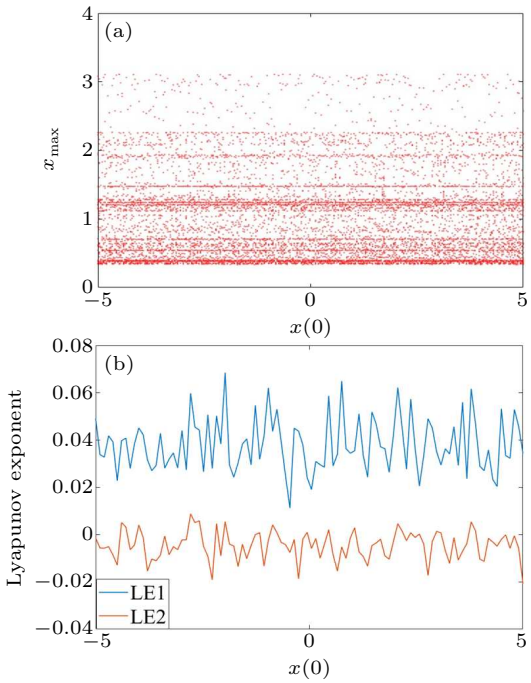


Fig. 11. Analysis of locally constant chaotic behavior of the system varying with $x(0)$: (a) bifurcation diagram, (b) Lyapunov exponent spectrum.

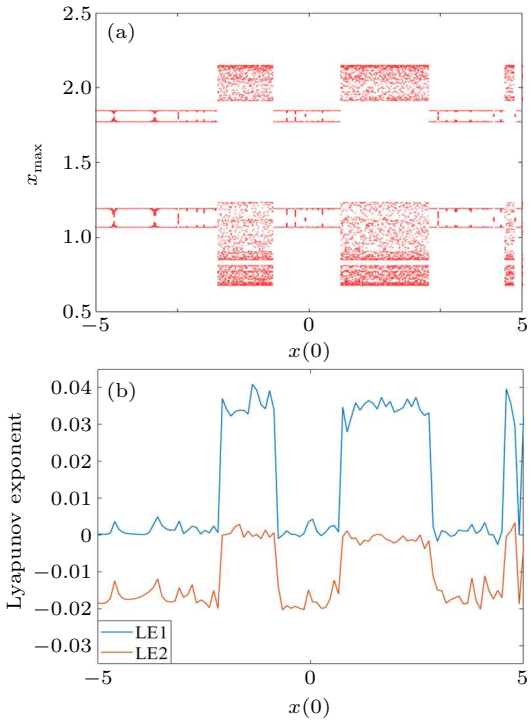


Fig. 12. Analysis of system state transitions with varying $x(0)$: (a) bifurcation diagram, (b) Lyapunov exponent spectrum.

chaotic states in the system's dynamics. Specifically, as increases from -3.25 to -0.12, the system switches from a periodic to a chaotic state, followed by locally constant chaotic behavior around $x(0) = -0.08$. Subsequently, the system returns to a periodic state with a periodic window in the range $(-0.8, 0.8)$, transitions again to a locally constant chaotic state for $x(0) \in (0.4, 1.8)$, and finally, after a period window in $x(0) \in (1.9, 3)$, the system switches back to a local constant chaotic state. These observations highlight that the sensitivity of the system's state-switching process is strongly dependent on initial conditions.

3.5. Offset boosting control

The proposed MHRN system (6) can implement compensation control on the state variable y by introducing an offset variable u, such that $y \to y + u$. Under this control, a hidden parameter shift phenomenon can occur within specific regions. By selecting an appropriate value for u, the system can effectively compensate for variations in y.

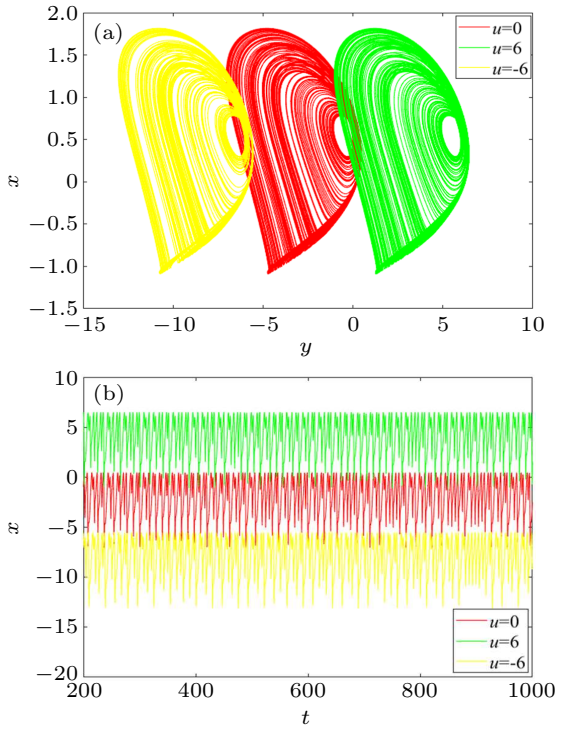


Fig. 13. Chaotic attractors and time series of state variable y under offset boosting with control parameter u: (a) phase diagram in the y–φ_m plane for $u = 0$ (red), $u = -6$ (green), and $u = 6$ (yellow); (b) time series of y for $u = 0$ (red), $u = -6$ (green), and $u = 6$ (yellow).

Specifically, consider the transformations $x \to x$, $y \to y + u$, and $\varphi_m \to \varphi_m$, where u is the offset boosting controller. Then, Eq. (6) can be rewritten as

$$\begin{cases} \dfrac{\mathrm{d}x}{\mathrm{d}t} = y + u - ax^3 + bx^2 + I + \beta\varphi_m \sinh(\alpha x), \\ \dfrac{\mathrm{d}y}{\mathrm{d}t} = c - dx^2 - (y + u), \\ \dfrac{\mathrm{d}\varphi_m}{\mathrm{d}t} = \mu x. \end{cases} \tag{7}$$

The system parameters for Eq. (7) are set as $a = 1$, $b = 3$, $c = 1$, $d = 5$, $\alpha = 0.8$, $\beta = 1.2$, $\mu = 0.535$, and $I = 0.3$. Under the initial condition $(0, 0, 0)$, the system exhibits a hidden parameter shift phenomenon as u varies from -6 to 6. Without loss of generality, we select $u = -6$, 0, and 6 as representative examples. Numerical simulations yield the phase diagram of the hidden parameter shift attractors in the y–φ_m plane, as shown in Fig. 13(a). These attractors demonstrate a linear distribution pattern with increasing values of the control parameter u. Furthermore, Fig. 13(b) presents the time series of the state variable y, further confirming this observed phenomenon.

4. Schematic diagram and circuit parameter selection

To validate the accuracy of the theoretical analysis, an equivalent circuit is designed, as illustrated in Fig. 14. The operational amplifier TL082CP is chosen with a ± 15 V power supply, while the multiplier employed is AD633JN.

In Fig. 14, the primary circuit of the MHRN model consists of two integrating channels, implementing the first and second equations of the system (6). According to Kirchhoff's current law, the circuit equations can be expressed as follows:

$$\begin{cases} RC_1 \dfrac{\mathrm{d}V_x}{\mathrm{d}t} = \dfrac{R}{R_{10}} V_y - \dfrac{g_1 g_2 R}{R_8} V_x^3 + \dfrac{g_2 R}{R_7} V_x^2 + \dfrac{R}{R_9} V_1 \\ \qquad\qquad + \dfrac{2RI_s R_5 g \varphi_m}{R_6} \sinh\left(\dfrac{R_4}{nV_T R_3} v_m\right), \\ RC_2 \dfrac{\mathrm{d}V_y}{\mathrm{d}t} = \dfrac{R}{R_{12}} V_2 - \dfrac{g_3 R}{R_{13}} V_x^2 - \dfrac{R}{R_{11}} V_y, \\ RC_3 \dfrac{\mathrm{d}V_{\varphi_m}}{\mathrm{d}t} = \dfrac{R_2}{R_1 R} V_x, \end{cases} \tag{8}$$

where V_1 and V_2 are the external bias voltages, and g_1, g_2, g_3, and g denote the gains of the multipliers. The variables V_x, V_y, and V_{φ_m} represent the capacitor voltages of the respective integrated circuit channels. By comparing Eqs. (8) and (6), the circuit components can be determined as

$$\begin{cases} R_{10} = R, \quad R_8 = \dfrac{g_1 g_2 R}{a}, \ R_7 = \dfrac{g_2 R}{b}, \ R_9 = \dfrac{V_1 R}{I}, \\ R_6 = \dfrac{2RI_s R_5 g}{\beta}, \ R_{12} = \dfrac{V_2 R}{c}, \ R_{13} = \dfrac{g_3 R}{d}, \ R_{11} = R. \end{cases} \tag{9}$$

A time scale factor of $RC = 10\ \mathrm{k\Omega} \times 100\ \mathrm{nF} = 1$ ms is adopted, where $R = 10\ \mathrm{k\Omega}$ and $C = 100$ nF. By normalizing the voltages as $x = V_x/1$ V, $y = V_y/1$ V, and $\varphi_m = V_{\varphi_m}/1$ V, and setting $g_1 = g_2 = g_3 = g_4 = 1$, the remaining circuit parameters can be calculated according to Eq. (9) and are summarized in Table 2.

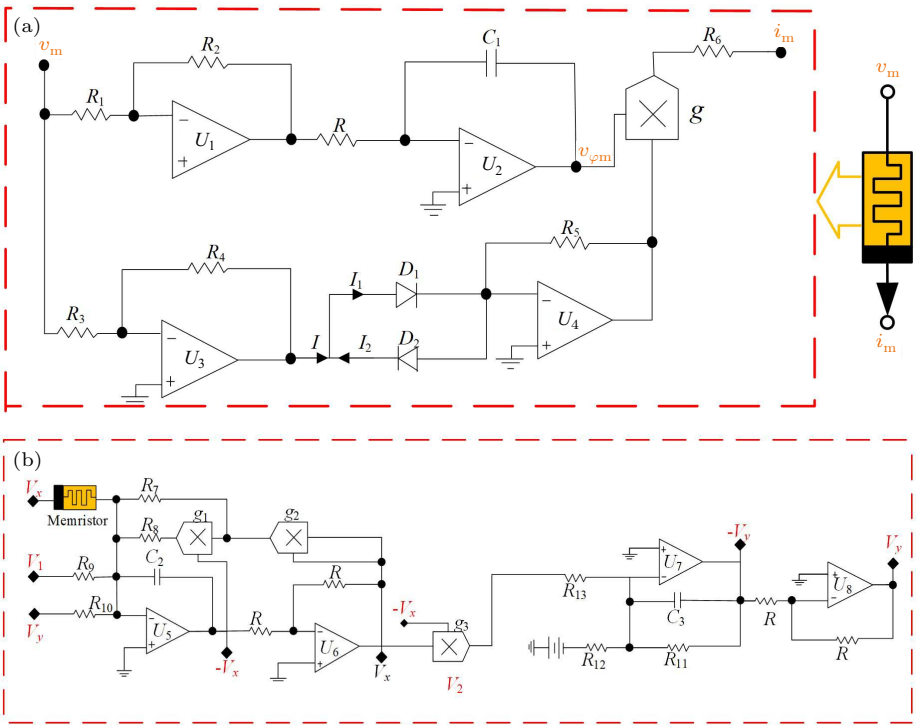


Fig. 14. The circuit schematic diagram of the proposed MHRN model.

Table 2. Circuit parameters of the proposed MHRN model.

Parameters	Values	Parameters	Values
R_7	3.33 kΩ	R_{13}	2 kΩ
R_8	10 kΩ	V_1	1.5 V
R_9	adjustable	V_2	1.5 V
R_{10}	10 kΩ	R_{11}	10 kΩ
R_{12}	15 kΩ	R_6	adjustable

5. Experimental results

Based on the circuit schematic shown in Fig. 14, simulation verification is carried out using Multisim 14.0 software. The circuit parameters are listed in Table 2, where R_6 and R_9 serve as adjustable components corresponding to β and I in Eq. (6). The initial voltages of the capacitors ($V_x(0)$, $V_y(0)$, $V_{\varphi_m}(0)$) represent the initial conditions of the system.

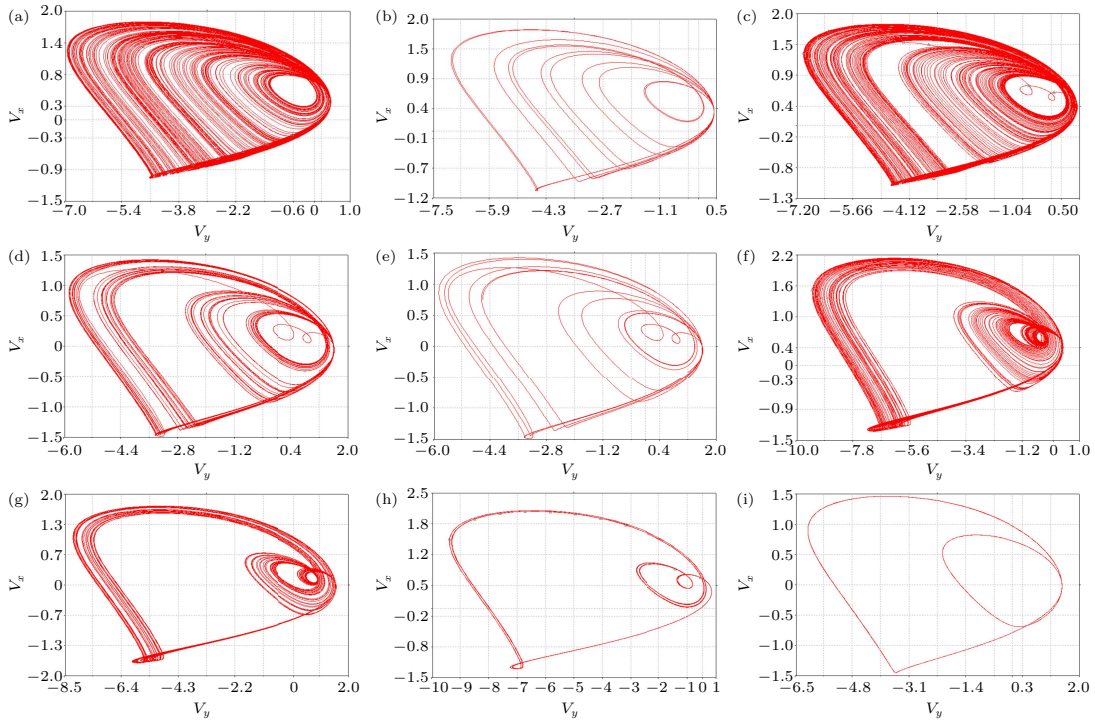


Fig. 15. Experimental phase trajectories illustrating the effect of current I on system dynamics for different values of R_9: (a) $R_9 = 48.39$ kΩ, (b) $R_9 = 42.49$ kΩ, (c) $R_9 = 41.67$ kΩ, (d) $R_9 = 38.46$ kΩ, (e) $R_9 = 37.5$ kΩ, (f) $R_9 = 31.25$ kΩ, (g) $R_9 = 30$ kΩ, (h) $R_9 = 27.27$ kΩ, (i) $R_9 = 25$ kΩ.

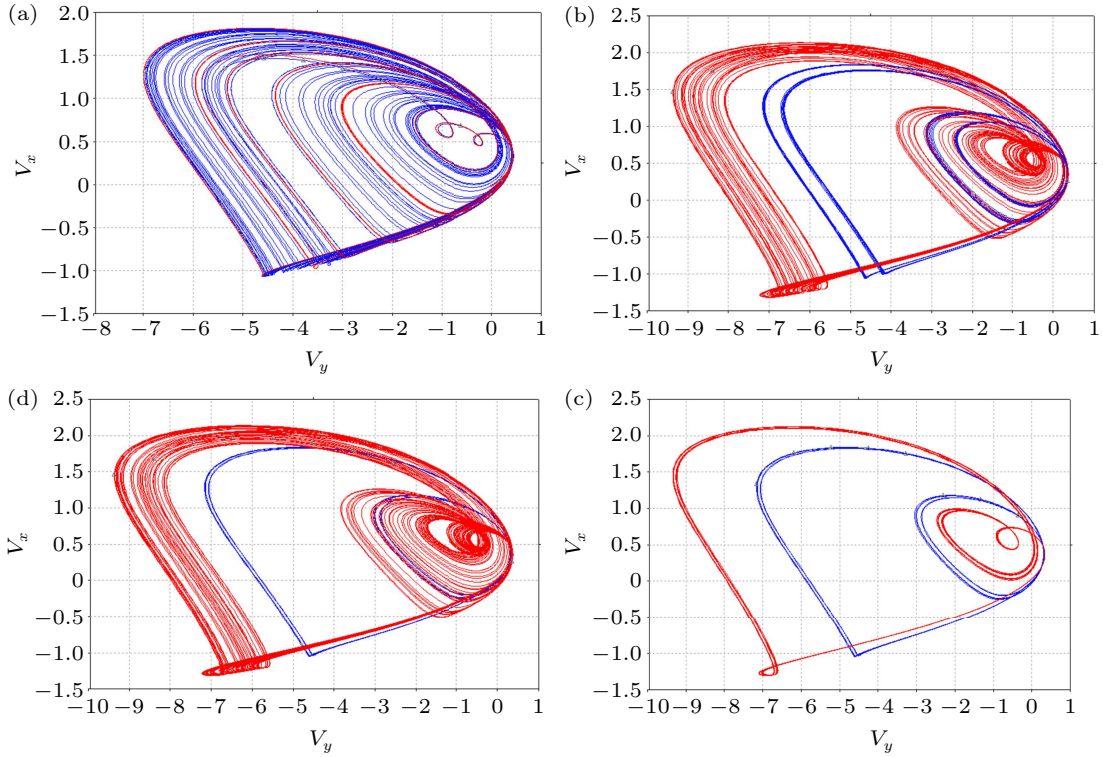


Fig. 16. Coexisting attractors observed in the circuit implementation for different values of R_9: (a) $R_9 = 42.49$ kΩ, (b) $R_9 = 31.25$ kΩ, (c) $R_9 = 30$ kΩ, (d) $R_9 = 27.27$ kΩ.

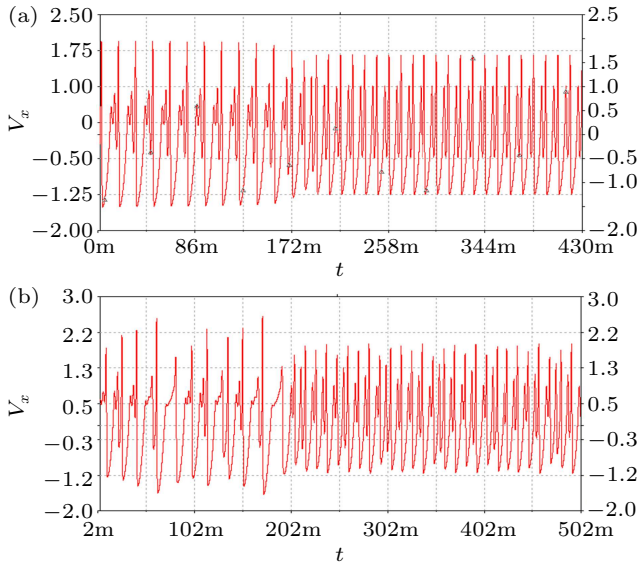


Fig. 17. Circuit realization of various neuronal signals: (a) transient chaos with initial capacitor voltages (−3 V, 0 V, 0 V), $R_9 = 8.368$ kΩ, $R_6 = 29.3$ kΩ; (b) transient chaotic transition with initial capacitor voltages (0 V, 0 V, 0 V), $R_9 = 7.69$ kΩ, $R_6 = 50$ kΩ.

When the capacitor initial voltages are set to (0.6 V, 0 V, 0 V) with R_6 fixed at 8.51 kΩ (corresponding to $\beta = 1.175$), the effect of the current I on the system dynamics is simulated by varying the resistance R_9. Figure 15 presents the V_y–V_x phase trajectories for different R_9 values, capturing a range of chaotic and periodic attractors.

Furthermore, by setting the capacitor initial voltages to (−5 V, 3 V, −1 V) while keeping $R_6 = 8.51$ kΩ constant, the coexistence of attractors at four different R_9 values is observed, as illustrated in Fig. 16. In addition, by varying the initial voltages, R_9, and R_6 according to the same methodology, transient chaos, transient chaotic transitions, and normal neuronal signals are successfully captured, as shown in Fig. 17.

6. Conclusion

In this work, an emulator corresponding to the TTC physical memristor mathematical model was designed, and a novel 3D HR neuron model was constructed based on the TTC memristor model. Through theoretical analysis, it was found that within a specific parameter region, the 3D memristive HR neuron model lacks an equilibrium point, thereby exhibiting hidden dynamic behavior. Comprehensive investigations using phase diagrams, bifurcation diagrams, and Lyapunov exponent spectra confirm that the proposed neuron model can manifest a wide range of dynamic phenomena, including coexisting attractors, transient chaotic dynamics, transient chaotic transitions, and offset-enhanced attractors. Furthermore, the model demonstrates pronounced sensitivity to initial conditions. Finally, an equivalent circuit implementation of the memristive HR neuron was developed, and its dynamic behavior was successfully verified through circuit simulations.

Acknowledgments

This work was supported by the Natural Science Foundation of Shandong Province (Grant No. ZR2024MF106), the National Natural Science Foundation of China (Grant Nos. 62371274 and 62401346), the China Postdoctoral

Science Foundation (Grant No. 2023M742138), the Natural Science Foundation of Shandong Province (Grant Nos. ZR2023MF004 and ZR2022MA073), the Postdoctoral Innovation Project of Shandong Province (Grant No. SDCX-ZG-202400311), the Natural Science Foundation of Qingdao Municipality (Grant No. 23-2-1-151-zyyd-jch), the Qingdao Postdoctoral Innovation Project (Grant No. QDBSH20230202012), and in part by the Elite Project of Shandong University of Science and Technology.

References

[1] Du Z, Li Z, Wang P, Zhuang Z and Liu Z 2022 *Int. J. Solids Struct.* **242** 111554
[2] Ma J 2025 *Nonlinear Dyn.* (in press)
[3] Singh A, Verma U, Mishra A, Yadav K, Sharma A and Varshney V 2024 *Chaos Solitons Fractals* **182** 114864
[4] Beyhan S 2024 *Chaos Solitons Fractals* **180** 114578
[5] Ding D, Chen S, Zhang H, Yang Z, Jin F and Liu X 2024 *Nonlinear Dyn.* **112** 10529
[6] Yang Y and Liao X 2019 *IEEE Trans. Neural Netw. Learn. Syst.* **30** 306
[7] Huang L, Wang S, Lei T, Huang K and Li C 2024 *Int. J. Bifurc. Chaos* **34** 2450022
[8] Chen D, Li J, Zeng W and He J 2023 *Cogn. Neurodyn.* **17** 203
[9] Slepukhina E, Bashkirtseva I, Kgler P and Ryashko L 2023 *Chaos* **33** 033106
[10] Moujahid A and Vadillo F 2022 *Chaos Solitons Fractals* **158** 112071
[11] Tezoh F, Adamou D and Fouda H 2023 *Phys. Scr.* **98** 115233
[12] Wu K, Zheng H and Li T 2022 *Discrete Dyn. Nat. Soc.* **2022** 8384444
[13] Afuwape O, Olafasakin O and Jiles D 2022 *IEEE Trans. Magn.* **58** 5800205
[14] Yan X, Li Z J and Li C L 2024 *Chin. Phys. B* **33** 028705
[15] Nefzi A, Orlacchio R, Carr L, Lemercier C, El Khoueiry C, Lewis N et al 2022 *IEEE Trans. Microw. Theory Techn.* **70** 1871
[16] Wan J Y, Wu F Q, Ma J and Wang W S 2024 *Chin. Phys. B* **33** 050504
[17] Lin H, Wang C and Tan Y 2020 *Nonlinear Dyn.* **99** 2369
[18] Njitacke Z, Tsafack N, Ramakrishnan B, Rajagopal K, Kengne J and Awrejcewicz J 2021 *Chaos Solitons Fractals* **153** 111577
[19] Zhang F, Shi H, Jié M, Wang L and Duan S 2022 *Int. J. Bifurc. Chaos* **32** 2250165
[20] Li Z, Zhou C and Wang M 2019 *AEU-Int. J. Electron. Commun.* **100** 127
[21] Lv M and Ma J 2016 *Neurocomputing* **205** 375
[22] Bao H, Hu A, Liu W and Bao B 2020 *IEEE Trans. Neural Netw. Learn. Syst.* **31** 502
[23] Zhang S, Zheng J, Wang X and Zeng Z 2021 *Chaos Solitons Fractals* **145** 110761
[24] Parastesh F, Rajagopal K, Jafari S and Perc M 2025 *Fractal Fract.* **9** 276
[25] Lin H, Wang C, Sun Y and Yao W 2020 *Nonlinear Dyn.* **100** 3667
[26] Yuan F, Li S, Deng Y, Li Y and Chen G 2023 *IEEE Trans. Ind. Electron.* **70** 4120
[27] Kaslik E 2017 *Fract. Calc. Appl. Anal.* **20** 623
[28] Yang F, Xu Y and Ma J 2023 *Chaos* **33** 023110
[29] Stenzinger R V and Tragtenberg M H R 2025 *Chaos* **35** 013132